Proceedings of the Sixteenth International Conference on
Computational Structures Technology
Edited by: P. Iványi, J. Kruis and B.H.V. Topping
Civil-Comp Conferences, Volume 14, Paper 10.3
Civil-Comp Press, Edinburgh, United Kingdom, 2026
ISSN: 2753-3239, doi: 10.4203/ccc.14.10.3


# Local Analysis of Nonlinear Elastomers Steadily Sliding over Rough Surfaces

**P. Le Tallec**

**Department of Mechanics, Ecole Polytechnique, Palaiseau, France**

## Abstract

A local analysis of nonlinear elastomers steadily sliding over rough surfaces at scales ranging from millimeters to micrometers is presently mostly restricted to materials in small strains governed by linear constitutive laws. Our goal herein is to extend this local approach in order to be able to handle large deformation and nonlinear viscoelastic constitutive laws. The basic constitutive model to be used for this purpose is fully incompressible and enters in the general class of parallel network models. It will be calibrated on available experimental data, using a minimal number of branches which is cost efficient compared to certain industrial models using dozen of branches. Moreover, it couples the different time scales, as might occur due to the evolution of the underlying microstructure, which cannot be done by the standard multi-branch models. We will then illustrate how this model can be used in large deformation first as a post treatment quantitatively evaluating the potential inaccuracies of the linear model, and second as the main constituent of a full nonlinear analysis of the problem.

**Keywords:** contact mechanics, viscoelastic materials, ground modeling, sliding, elastomers, multi-scale.

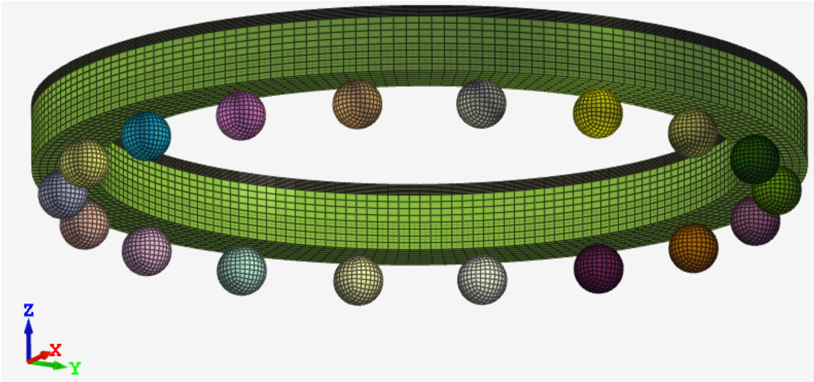


Figure 1: An example of a FE mesh for a time dependent direct contact simulation using a fully nonlinear viscoelastic model. Taken from [7]

# 1 Introduction

Predicting the tangential forces generated by the relative sliding of a tire on a rough road surface is challenging, because of the complex geometry of the tire pattern, the multiplicity of the geometric scales defining the road surface, and the complexity of the viscoelastic response of the constitutive material. Direct simulation can be performed at a macroscopic scale to handle the combined effect of the pattern's geometry, its large deformation and the nonlinear viscoelastic response of the constitutive material. They can also be compared as in [7] to various experimental results (Fig. 1).

But such approaches are presently restricted to problems with smooth obstacles and fail to handle the complexity of surface roughness down to the micrometer scale. The main strategy for handling these small scales introduce a model local problem which keeps the geometric complexity of the rough soil surface, but simplifies the problem by assuming small strains, treating the constitutive material as linear viscoelastic and the geometry of the contact region as a half-space; see, e.g., [2, 17, 21, 22, 24]. Citing [7], although this approach provides a computationally accessible methodology to estimate complex contact interactions, it is centered by construction on the assumptions of small strains and linear constitutive behavior, which are most often not satisfied in practice. We can see on Fig. 2 how the prediction of the contact interaction can be impacted by using nonlinear constitutive laws.

Our goal herein is to extend this local approach in order to be able to handle large deformation and nonlinear viscoelastic constitutive laws. The basic constitutive model to be used for this purpose is fully incompressible and enters in the general class of parallel network models as reviewed in [9] and introduced early in [16]. It will calibrated on available experimental data. It uses a minimal number of branches which is cost efficient compared to certain industrial models using a dozen of branches [12, 18]. Moreover, it couples the different time scales, as might occur due to the evolution of the underlying microstructure, which cannot be done by the standard multi-branch

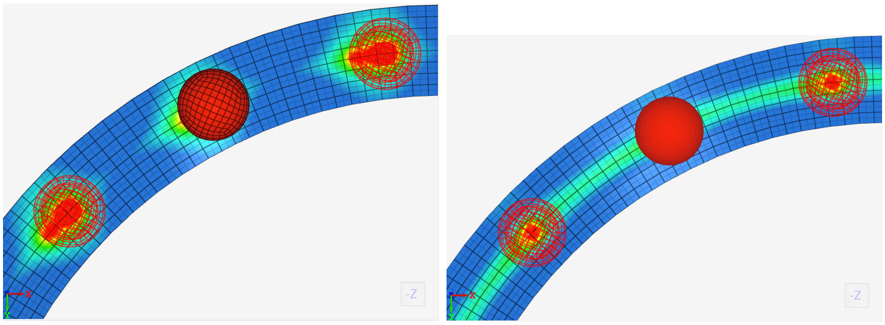

Figure 2: Contour plot of the predicted displacement component in the Z direction (bottom-eye view) at the specimen lower face-angular position during a rotating sliding experiment over smooth lubricated obstacles. The results pertain to the simulation based on the viscoelastic model respectively with linear (left) and nonlinear (right) viscosity. Taken from [7]

models. The preliminary tests of [7] did indicate the potential advantage of such a coupling, but it constitutes a challenge in the construction and solution of a relevant contact problem at small scale, since the nonlinearity forbids any a priori elimination of the internal displacement field.

The paper will be organized as follows. Section 2 reviews the classical linear model used for small scale contact [3,20]. The next section describes and calibrates a relevant nonlinear viscoelastic constitutive law which has the potential of coupling different time scales. Section 4 explains how the classical model can be updated to handle this multiscale constitutive law and the potential large deformation of the polymer. We will first illustrate how this nonlinear model in large deformation can be used as a post treatment for evaluating the potential inaccuracies of the linear model. The remaining problem will then be to develop an efficient nonlinear solver and to properly couple such local problems to a full field macroscopic simulation.

# 2 The classical linear local model of an elastomer sliding over a rough surface

## 2.1 Description of the local problem

In a classical approach [17], [20], the friction law is obtained by considering a semi infinite horizontal slab of viscoelastic elastomer sliding at a constant velocity $\underline{V} = V\underline{e}_x$ over a rough periodic soil of elevation

$$z = h(x,y) = \sum_{|n,m| \leq n_{max}} h_{nm} e^{2i\pi(nx/L_x + my/L_y)}.$$

The soil is often assumed to be fractal meaning that the high frequency amplitude of the soil oscillation follows a power law $|h_{nm}| \approx L(L|n,m|)^{-\alpha}$, where $|n,m| =$

$2\pi\sqrt{n^2/L_x^2 + m^2/L_y^2}$ denotes the associated spatial frequency and where the fractal exponent $\alpha$ and the cut off frequency $n_{max}$ are given descriptors of the soil [13], [17], to be used in the construction of this Fourier series [13], [24]. The slab is supposed to penetrate of a given distance $\delta z$ with respect to the highest point $h_{max}$ of the soil, through the imposition of an unknown pressure $p_0$ applied at infinity. A frictionless contact is assumed between the soil and the elastomer.

## 2.2 Constitutive assumptions and fundamental solution

The material is supposed to be istropic, incompressible and linearly viscoelastic with a viscoelastic shear modulus given in the frequency domain by a given complex function $G(\omega)$. In soil related coordinates $\underline{x} = \underline{X}_m - \underline{V}t$, ($\underline{X}_m$ denoting the material coordinates), the solution is supposed to be in small strains, periodic and steady (no explicit dependence on time). Moreover, it is assumed that at first order the soil reaction will be mainly vertical $\boldsymbol{\sigma} \cdot \boldsymbol{n} = p(x, y)\underline{e}_z$ reducing the contact conditions to be satisfied at each point $(x, y, 0)$ of the lower surface $z = 0$ to

$$u_z \geq h - h_{max} + \delta z, p \geq 0, (u_z - h + h_{max} - \delta z)p = 0.$$

Under these assumptions, the solution of the problem is classically given in Fourier form [20] by

$$p = p_0 + \sum_{|n,m| \neq 0} p_{nm} e^{2i\pi(nx/L_x + my/L_y) - |n,m|z}$$

$$u_z(x, y, z) = \delta z + \sum_{|n,m| \neq 0} \frac{p_{nm}}{|n, m| G(nV/L_x)} (1 + |n, m|z) e^{2i\pi(nx/L_x + my/L_y) - |n,m|z}.$$

The other components of displacement and the deviatoric part of the stress have similar expressions while vanishing at $z = 0$ and at infinity.

The unknown coefficients $p_0$ and $p_{nm}$ are obtained by solving the above contact conditions by an active set strategy. The idea is to guess the surface of contact. Once this surface given, we solve the linear problem of finding the point wise pressure in the surface of contact generating a local displacement $u_z = h - h_{max} + \delta z$ bringing the slab onto this surface, where $u_z$ is to be given by the above Fourier series. A direct solver can be used there since the corresponding matrix is the restriction on the active set of the transfer matrix $p(x, y, 0) \rightarrow u_z(x, y, 0)$ to be computed line by line by Fast Fourier Transform. $p(x, y, 0) \rightarrow p_{nm}$ (FFT) $p_{nm} \rightarrow u_{nm}$ (local multiplication) $u_{nm} \rightarrow u_z(x, y, 0)$ (inverse FFT). Then, the active set is corrected by removing the points where the pressure is negative and adding the points where the displacement violates the non interpenetration condition. A matrix free method can also be used ( [3]).

### 2.3 Post treatment of the friction coefficient

The macroscopic friction force is obtained by observing that the pressure used in the solution process is vertical and hence not normal to the soil surface. A correcting term must be added. It assumes that the pressure obtained above is only the vertical component $p_z$ of the real reaction force density which is applied normally to the soil surface when assuming a local frictionless contact. There must therefore be an horizontal part of the reaction force density $p_x = p_z \tan\theta$ with $\theta$ the angle of the soil surface with the vertical in the plane $(x, z)$. But since the body is in contact with the soil, this tangent is also the slope of the deformed configuration of the elastomer, which yields [8]

$$p_x = p_z \frac{\partial u_z}{\partial x}.$$

Once integrated and averaged over the space period, we get the classical formula [19]

$$T_x = 2 \sum_{(n,m)>0} G"(nV/L_x) \frac{n/L_x}{|n,m|} \left| \frac{p_{nm}}{G(nV/L_x)} \right|^2$$

This is the formula of [17] but to be used with the numerically obtained Fourier coefficients $p_{nm}$.

### 2.4 Discussion

This approach predicts the normal pressure $p_0$ and the friction force density $T_x$ which must be imposed at a macroscopic scale in order to achieve a given penetration at a given sliding velocity. In practice, it does produce nice qualitative results (Fig. 3) and seems to be rather predictive.

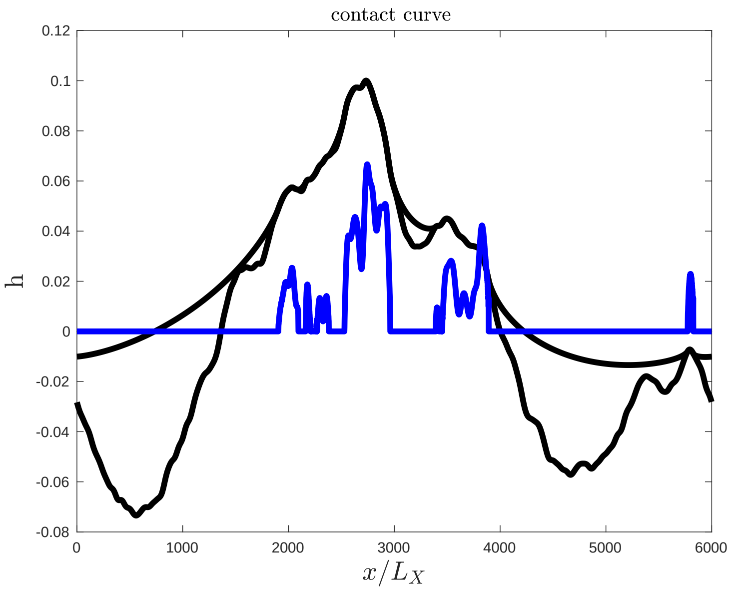


Figure 3: A typical output of a linear model prediction. The top curve represents the bottom surface of the solid, the middle curve the soil surface and the blue bottom one the pressure distribution. In this 2D simple case run with a space period $L_X = 10\,cm$, a velocity $V = 1\,cm/s$, a soil cut off wave length of $0.1\,mm$, a highest soil elevation $h_{max} = 1\,cm$, an imposed penetration $\delta z = 8\,mm$, that is eighty percent of the maximal elevation, we have used 6000 spatial points for the space discretization, that is at minimum 60 points per soil wavelength. The storage coefficient $G'$ did vary from $1.6$ Mpa at $0.1$ Hz to a maximal value of $3$ MPa at $100$ Hz, while the loss modulus did vary from $0.5$ MPa to $1.9$ MPa. The active set strategy did converge in $54$ iterations, predicting a normal pressure and horizontal friction respectively of $28.53$ kPa and $8.36$ kPa, yielding a friction coefficient close to $\mu = 0.3$.

Nevertheless, in the context of large deformation and of nonlinear viscoelastic materials, there are a few assumptions which are questionable and therefore should be challenged in a more general framework : (i) it uses a linear, frequency dependent, isotropic relations between the strain tensor and the Cauchy stress, (ii) it uses the linearized strain tensor in the construction of the analytical solution, hence assuming small strains, (iii) it assumes that the horizontal component of the reaction force does not influence the steady state equilibrium of the the structure.

# 3 Introduction and calibration of a generic nonlinear constitutive model

## 3.1 Reference model

To go further, we will use herein an incompressible nonlinear viscoelastic model, belonging to the class of parallel network models as reviewed in [9] and introduced early in [16]. In addition of the internal pressure $p_h$ ensuring the incompressibility constraint, it use three components : i) a nonlinear hyperelastic branch $\cdot_{Eq}$ to be fitted on multistep relaxation tests (MSR), (ii) a single nonlinear viscoelastic branch $\cdot_v$ based on a standard multiplicative decomposition of the deformation gradient, with a viscosity constructed as a nonlinear function of the viscous deformation rate and amplitude, (iii) a linear viscoelastic branch $\cdot_{HF}$ with constant viscosity and stiffness, fitted so that to recover the results of the DMA tests at 100Hz.

The Cauchy stress tensor is therefore given by

$$\boldsymbol{\sigma} = \boldsymbol{\sigma}_{Eq} + \boldsymbol{\tau}_v + \boldsymbol{\tau}_{HF} - p_h \mathbf{Id},$$

with an evolution of the viscous deformations $\mathbf{C}_v$ and $\mathbf{C}_{HF}$ of the viscoelastic branches governed by

$$\mathbf{d}_v = \eta^{-1} \boldsymbol{\tau}_v, \quad \mathbf{d}_{HF} = \eta_{HF}^{-1} \boldsymbol{\tau}_{HF}. \tag{1}$$

As usual in presence of a multiplicative splitting, the viscous strain rate in the present configuration is given by $\mathbf{d}_v = \sqrt{\mathbf{C}_v^{(-1)}} \dot{\mathbf{C}}_v \sqrt{\mathbf{C}_v^{(-1)}}$ with a similar expression for $\mathbf{d}_{HF}$. For simplicity, the model will be used with a free energy function only depending on the first invariants of the dilatation tensors $I_1 = Tr(\mathbf{C}) = Tr(\mathbf{B})$ and $I_1^e = Tr(\mathbf{C}_e) = Tr(\mathbf{B}_e)$ yielding

$$\begin{aligned}
\boldsymbol{\sigma}_{Eq} &= \mu \left( \left( \frac{I_1}{3} \right)^{\alpha - 1} + c \left( \frac{(I_1^+)^2}{10} + \frac{I_1^+}{1 + d I_1^+} \right) \right) \mathbf{B}, &(2)\\
\boldsymbol{\tau}_v &= m \left( \frac{I_1^e}{3} \right)^{a-1} \operatorname{dev} \left( \mathbf{B}_e \right), &(3)\\
\boldsymbol{\tau}_{HF} &= m_{HF} \operatorname{dev} \left( \mathbf{F} \mathbf{C}_{HF}^{(-1)} \mathbf{F}^T \right). &(4)
\end{aligned}$$

relating the Cauchy stress tensor to the Finger tensors $\mathbf{B} = \mathbf{F}\mathbf{F}^T$ and $\mathbf{B}_e = \mathbf{F}\mathbf{C}_v^{(-1)}\mathbf{F}^T$. A correction term in $I_1^+ =$ is added to the elastic energy to improve the fitting of the long term elastic modulus. Many other choices can be used there. In any case, the present work does not focus on this equilibrium branch, but on the impact of the nonlinear viscous laws proposed in [7] or in [1] $\eta = \eta_0 \eta^\omega(J^*)\eta^\times(I_1^v)$ to be identified as a nonlinear function of viscous deformation $I_1^v$ and viscous deformation rate $J^*$. Observe that such a nonlinearity introduces a coupling between different time scales. Such models base their measure of the viscous deformation rate on the creep flow rule by adimensioning the inelastic deviatoric Kirchhoff stress

$$J^* = \frac{1}{m}\|\boldsymbol{\tau}_v\|.$$

Herein, we use a combination of the choices introduced respectively in [7] and in [1]

$$\eta = \eta_0 \frac{1 + q_2(k_* J^*)^{2\beta_2}}{1 + (k_* J^*)^{2\beta_2}} \left(1 + k_1(\sqrt{I_1^v/3} - 1)\right)^{\beta_1},$$

with $q_2 \ll 1$ combining a shear thinning effect at large deformation rate $J^*$ and a shear thickening at large amplitude $I_1^v/3$.

## 3.2 Calibration strategy

The 13 constitutive coefficients of our model fall in four categories :

(i) four coefficients describe the equilibrium branch, namely the reference elastic shear modulus $\mu$, the negative exponent $\alpha$ controlling the softening at moderate extensions, and the adimensional corrector terms $c$ and $d$ to induce stiffening at larger extensions. The elastic shear modulus is obtained in a small amplitude extension test, the exponent $\alpha$ , and correctors $c$ and $d$ are obtained through a least square fitting of the equilibrium stresses observed in a multistep relaxation test;

(ii) four coefficients control the dynamic over-stress and creep at small amplitude, which are the viscoelastic shear modulus $m$, the reference viscosity $\eta_0$ (or equivalently the reference relaxation time $\tau_0 = \eta_0/m$), the scaling factor $k_*$ defining the lower limit of the nonlinear regime in terms of the deformation rate, and the exponent $\beta_2$ of the power law used in this regime to introduce a reduction of viscosity at large deformation rates. The last coefficient $q_2$ entering the viscosity law $\eta^\omega(J^*)$ of [7] introduces a lower bound for viscosity at high deformation rates, but its physical impact is limited due to the presence of the high frequency branch. It is essentially a regularization factor to be set to a very small value for numerical purposes. These coefficients are obtained by least square fitting of the storage and loss moduli measured at three reference frequencies and at a reference amplitude of $\gamma = 0.1$. The predicted values of the storage and loss moduli at frequency $j$ are obtained from the Fourier transform of the stress signal as computed by the proposed model during a stabilized cycle;

(iii) three coefficients characterize the shear thickening expected at large amplitude, namely the negative exponent $a$ controlling the softening of the viscoelastic stiffness at moderate extensions, the scaling factor $k_1$ defining the lower limit of the nonlinear regime in terms of the deformation amplitude, and the exponent $\beta_1$ of the power law used in this regime to describe the increase of viscosity with the deformation amplitude. These coefficients are obtained by a least square fitting of the time history of the stresses as observed in a multistep relaxation test (MSR) and in an uniaxial loading/unloading test (CD), least square fitting which also allows to update the reference relaxation time $\eta_0$. In [7], the power law is replaced by an homographic expression introducing an upper bound $q_1$ in terms of viscosity, but in practice, this variant does not improve the quality of our predictions;

(iv) two coefficients are associated to the high frequency branch, namely a constant viscoelastic stiffness $m_{HF}$ and a constant viscosity $\eta_{HF} = m_{HF}\tau_{HF}$. They are specified by fitting the results of the DMA test at 100 Hz. Other linear branches can be added with even lower time scales if needed.

| | | | | |
|---|---|---|---|---|
| $\mu = 0.7MPa$ | a=-7 | c=1.09 | d= 0.734 | |
| $m = 2.06MPa$ | $\tau_0 = 8.5s$ | $m_{HF} = 5.6MPa$ | $\tau_{HF} = 4.8E-4s$ | |
| $\alpha = -1.7$ | $k_* = 23.2$ | $\beta_2 = 3.13$ | $k_1 = 58.7$ | $\beta_1 = 1.16$ |

Table 1: Constitutive coefficients obtained by fitting available experimental results [7]

## 3.3 Prediction results on standard tests

The results of this calibration procedure as applied to the reference model are displayed in Figure 4 and Figure 5.

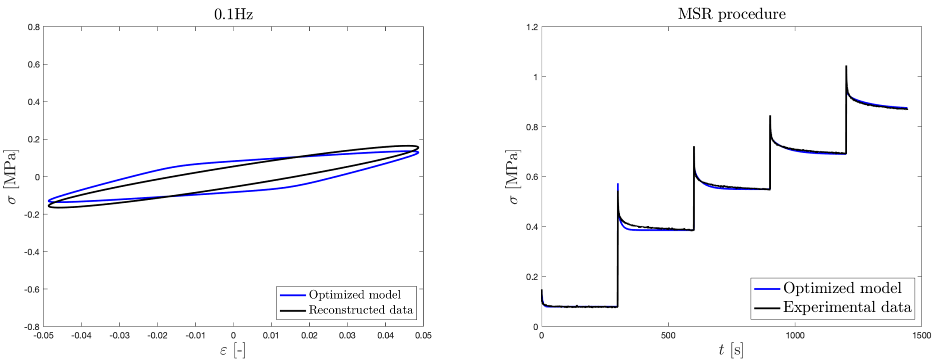


Figure 4: Prediction of the reference optimized model on the fitting tests. The upper figure displays in blue the stress vs shear curve as predicted at 0.1 Hz, compared to the results (in black) of the corresponding linear model using the experimental values of the storage and loss modulus, the bottom curve display the time history of the stress as predicted by the model (in blue) and as observed (in black) for the multistep relaxation step (MSR). Observe that the nonlinear viscous law does induce a non elliptical response at low frequency in the dynamic test.

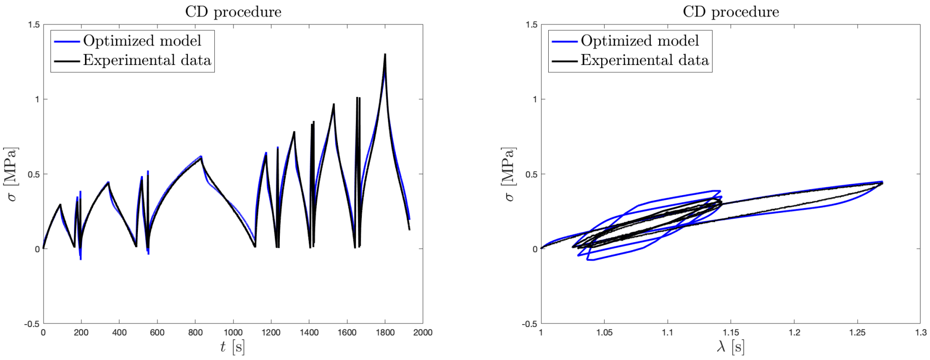


Figure 5: Detailed comparison of the predicted and observed results for the CD test. Predicted values in blue and experimental values in black. The top figure displays the time history of the axial engineering stress. The bottom curve display the same engineering stress as function of the elongation in the CD test. The global results are quite satisfactory, but the predicted model may present rather abrupt change of slopes when the nonlinearity is triggered, which are not observed in the experimental tests. Observe also an excess of viscosity in the predicted model at low deformation rate.

To understand the impact of the nonlinearity and the associated time scale coupling, Table 2 display the (four orders of magnitude) range of variations of the inverse viscosity and of its arguments as predicted by the optimized model in the different experiments. The two last columns display the difference between the experimental and predicted storage and loss modulus at difference frequencies. As stated earlier, at low frequency with this single nonlinear branch, the model underestimates the storage modulus and overestimates the loss modulus, while the predictions are much more accurate at high frequencies.

| | $\min \eta^{-1}$ | $\max \eta^{-1}$ | $\max(J_*)$ | $\max(\sqrt{\frac{I_1^v}{3}} - 1)$ | $\delta G'$ | $\delta G$" |
|---|---|---|---|---|---|---|
| $0.1Hz$ | $1.11E-01$ | $7.55E-01$ | $3.18E-01$ | $8.84E-04$ | $3.40E-01$ | $-1.96E-01$ |
| $1Hz$ | $1.14E-01$ | $5.17$ | $4.42E-01$ | $5.34E-04$ | $1.38E-01$ | $-1.59E-01$ |
| $10Hz$ | $1.16E-01$ | $3.09E+01$ | $5.91E-01$ | $2.54E-04$ | $2.90E-02$ | $1.23E-02$ |
| $100Hz$ | $1.17E-01$ | $1.14E+02$ | $7.32E-01$ | $5.17E-05$ | $-7.74E-04$ | $-5.87E-04$ |
| CD | $3.31E-03$ | $4.71$ | $6.35E-01$ | $3.58E-01$ | | |
| MSR | $4.47E-03$ | $5.25$ | $6.20E-01$ | $2.72E-01$ | | |

Table 2: Range of inverse viscosity, a-dimensional deformation rate, viscous extension as predicted in the different tests with the calibrated reference model. The two last columns display the difference between the experimental and predicted storage and loss modulus at difference frequencies. At low frequency, with this single nonlinear branch, the model underestimates the storage modulus and overestimates the loss modulus, while the predictions are much more accurate at high frequencies.

## 3.4 Potentialities and limits of the model

Although quite efficient, the fitting is not optimal at two levels. First, when trying to cover three order of magnitude of frequencies with a single nonlinear branch, the low frequency prediction (at $0.1$ Hz) is too low for the stiffness modulus $G^*$ $(1,41$ MPa instead of $1,7$ MPa) and too high for the loss modulus $G$" $(0,74$ MPa instead of $0,56$ MPa). Moreover, although the global history of the stress is well predicted, the detailed comparison of the predicted and observed results for the CD test displayed in Figure 5 shows that the reduction of relaxation time is too sharp when transiting from a small deformation rate (as encountered in the peak of elongations) to a larger one, which induces rather abrupt changes of slope in the stress evolution. The results are similar when one using the model of [1], with an additional drawback of the latter. In the MSR test, the power law of the Bergstrom model forbids any relaxation at low deformation rate, freezing the sample in an unphysical unrelaxed state.

Our calibration ignored Payne effects, using a single amplitude in the dynamic shear tests and calibrating the strain amplitude effect on uniaxial tests run at large elongations, and therefore removing any potential sensitivity of the nonlinear viscosity at small amplitudes. The optimized model is sensitive to the amplitude of the dynamic shear test used for calibration, but changing the amplitude in the calibration had a rather limited impact, and is unable to predict the proper variations of the storage and loss moduli at small amplitudes, as observed on dynamic shear tests run on filled rubbers. A different possibility is to calibrate the amplitude dependance of the model by using the results of dynamic tests run at different amplitudes and frequencies. This leads to a better cross fitting of the moduli $G^*$ but at the cost of a questionable aspect of the stress to strain curves as predicted in dynamic shear tests, and at poorer results on the uniaxial tests. We can therefore conclude that nonlinear viscous laws as used herein do not have the proper scope for describing Payne effects. More sophisticated laws would be needed there, to be inspired from a deeper study of the evolution of the underlying microstructure in those tests.

Nevertheless, we think that the above model, because of its inherent nonlinearity and of the quality of the present fitting, is a good candidate for studying the impact of a nonlinear viscoelastic law on the output of a local contact model.

# 4 Developing a nonlinear local model of contact

## 4.1 Geometry and assumptions

We now want to develop a local contact problem, which does not suffer from the a priori restrictions of the linear model. For this purpose, we again consider an horizontal slab of viscoelastic elastomer sliding at a constant velocity $\underline{V} = V\underline{e}_x$ over a rough periodic soil of elevation $z = h(x, y)$. The soil is assumed to be fractal meaning that the high frequency amplitude of the soil oscillation follows a power law The slab is supposed to penetrate of a given distance $\delta z$ with respect to the highest point $h_{max}$ of the soil. A frictionless contact is assumed between the soil and the elastomer. In soil related coordinates $\underline{X} = \underline{X}_m - \underline{V}t$, the solution is again periodic and steady (no dependence on time). But we now assume that we are in large strains, taking into account the full nonlinear contact condition in the equilibrium equations, and that the material is governed by the nonlinear constitutive law calibrated in the previous section. And, in line with a potential use of this local model in a nonlinear homogenization strategy or within a domain decomposition strategy [11], the far field is located at a distance $L_z$ of the bottom, and is subjected to an imposed horizontal velocity, generating a shear force equilibrating the horizontal component of the soil reaction force.

## 4.2 Approximation strategy

Because on the nonlinear structure of the equilibrium equations and of the constitutive laws, it is no longer possible to develop an analytical solution for the solution as function of the surface traction. We thus need to use an approximation strategy for the displacement and pressure inside the slab. Different approximations are possible. An attractive one is to combine a finite element approximation in $Z$ and a Fourier expansion in $X$ and $Y$ in the form

$$\underline{u} = \sum_{\alpha,k,n,m} u_\alpha^{knm} \phi_k(Z) e^{2i\pi(nX/L_x + mY/L_y)} \underline{e}_\alpha$$

with test function $\phi_{kmn}(X, Y, Z)\underline{e}_\alpha = \phi_k(Z)e^{2i\pi(nX/L_x+mY/L_y)}\underline{e}_\alpha$, where $\alpha$ denotes the direction $x$, $y$ or $z$, and $k$ denotes the index of the finite element node in $Z$. The equilibrium problem reduces then to a set of nonlinear equations

$$\int_\Omega \boldsymbol{P}_{\alpha\beta}\phi_{kmn,\beta} dX dY dZ + \int_{Z=0} p\, \boldsymbol{n}_\alpha \phi_{kmn} dX dY = 0, \forall \alpha, k, m, n$$

with unknowns $\{u_\alpha^{knm}\}_{\alpha,k,n,m}$ and where $\boldsymbol{P} = J\boldsymbol{\sigma}\boldsymbol{F}^{-T}$ denotes the first order Piola Kirchhoff stress tensor. Each of these integrals are obtained by Gaussian integration along the vertical direction (at Gaussian weights and points $c_G$ and $Z_G$) and FFT along the horizontal directions (with equidistant spatial points $(X_i, Y_j)$). Typically, the deformation gradients at altitude $Z_G$ are obtained by inverse FFT in $X$ and $Y$

$$\begin{aligned}
\boldsymbol{F}(X_i, Y_j, Z) &= \mathbf{Id} + \sum_{\alpha,k,n,m} u_\alpha^{knm} e^{2i\pi(nX_i/L_x + mY_j/L_y)} \underline{e}_\alpha \otimes \underline{e}_{knm}(Z), \\
\underline{e}_{knm}(Z) &= 2i\pi\phi_k(Z)(\frac{n}{L_X}\underline{e}_X + \frac{m}{L_Y}\underline{e}_Y) + \phi_k'(Z)\underline{e}_Z.
\end{aligned}$$

The internal variable is next computed line by line at given $Y_j$ and $Z_G$ by finding the periodic solution of (1) with given deformation gradient $\{\boldsymbol{F}(X_i, X_j, Z_G)\}_{i=1,N}$. The constitutive laws (2-4) can then be locally applied at each point $(X_i, X_j, Z_G)$, which gives access to the Fourier coefficients $\hat{\boldsymbol{P}}^{nm}(Z_G)$ by direct FFT, reducing the above integral to the local sum

$$\int_\Omega \boldsymbol{P}_{\alpha\beta}\phi_{kmn,\beta} dX dY dZ =$$
$$\sum_{Z_G} c_G \left( 2i\pi\phi_k(Z_G) \left( \frac{n}{L_X}\hat{\boldsymbol{P}}^{nm}_{\alpha X}(Z_G) + \frac{m}{L_Y}\hat{\boldsymbol{P}}^{nm}_{\alpha Y}(Z_G) \right) + \phi'_k(Z_G)\hat{\boldsymbol{P}}^{nm}_{\alpha Z}(Z_G) \right).$$

A reduced integration is used for the hydrostatic pressure term, obtained by a penalty treatment $p_h(X_i, X_j, Z_s) = -\kappa(\det \boldsymbol{F}(X_i, X_j, Z_s) - 1)$ of the incompressibility condition to be imposed at attitudes $Z_s$. Finally the soil pressure $p(X_i, Y_j)$ representing the soil pressure at point $\underline{x} = \underline{X} + \underline{u}(\underline{X})$ with upward soil normal $\boldsymbol{n}(\underline{x})$ is obtained from the contact conditions

$$u_z(\underline{X}) \geq h(\underline{X} + \underline{u}(\underline{X})) - h_{max} + \delta z, p(X, Y) \geq 0, (u_z - h + h_{max} - \delta z)p = 0,$$

using typically an augmented Lagrangian approach [15]. The difference with the linear model is that the contact conditions are expressed in the deformed configuration, and that the contact force is applied along the soil normal and not vertically.

Computing the residuals for a given contact preserving displacement field is very fast and will be illustrated at the conference. This gives access to a qualification strategy of the results of the linear model. A challenge is next to find an efficient nonlinear solver, taking advantage of the fast evaluation of residuals.

## Acknowledgements

This paper was finalized during a stay of the author at the Oden's Institute for Computational Engineering and Sciences (U.T. Texas) within the J.T. Oden Visitors Program.

# References

[1] J.S. Bergstrom, M. Boyce, Constitutive modeling of the large strain time-dependent behavior of elastomers. J. Mech. Phys. Solids, vol 46, pp 931–954. 1998.

[2] R. Bugnicourt, Simulation of the contact between a rough surface and a viscoelastic material with friction, Ph.D. thesis. Université de Lyon, 2017.

[3] R. Bugnicourt, P. Sainsot, N. Lesaffre, A.A. Lubrecht, Transient frictionless contact of a rough rigid surface on a viscoelastic half-space, Tribology International, vol. 113, pp. 279–285, 2017.

[4] G. Carbone, F. Bottiglione, Asperity contact theories: do they predict linearity between contact area and load?. J Mech Phys Solids, vol. 56(8), pp. 2555–72, 2008.

[5] R.M. Christensen, Theory of Viscoelasticity, Dover Publications, Mineola, 2010.

[6] M. de Lorenzo, Multi-scale analysis of the tire grip on wet roads. Ph.D. thesis. Ecole Polytechnique, 2024.

[7] M. de Lorenzo, P. Le Tallec, O. Lopez-Pamies, P. Bussetta, Filled elastomers sliding over smooth obstacles: Experiments and modeling in large deformations, J. Mech. Phys. Solids, 2025.

[8] I.G. Goryacheva, F.I. Stepanov, E.V. Torskaya, Sliding of a smooth indentor over a viscoelastic half-space when there is friction, Journal of Applied Mathematics and Mechanics, vol. 79, pp. 596–603, 2015.

[9] F. Gouhier, J. Diani, A comparison of finite strain viscoelastic models based on the multiplicative decomposition, European. J. of Mech./ A Solids, vol. 108, 2024.

[10] K. Ghosh, S. Shrimali, A. Kumar, O. Lopez-Pamies, The nonlinear viscoelastic response of suspensions of rigid inclusions in rubber: I — Gaussian rubber with constant viscosity, Int. J. Solids Struct, vol. 154, pp 104544, 2021.

[11] C. Hager, P. Hauret, P. Le Tallec, B. Wohlmuth : Solving dynamic contact problems with local refinement in space and time, Computer Methods in Applied Mechanics and Engineering, Vol. 201-204, pp. 25-41, 2012

[12] P. Haupt, A. Lion, On finite linear viscoelasticity of incompressible isotropic materials, Acta Mecanica, vol. 159, pp 87–124, 2002

[13] Y.Z.Bu, K. Tonder, Simulation of 3-D random rough surface by 2-D digital filter and fourier analysis. Int J Mach Tools Manuf, vol. 32(1–2), pp. 83–90, 1992.

[14] A. Kumar, O. Lopez-Pamies, On the two-potential constitutive modeling of rubber viscoelastic materials, Comptes Rendus Mécanique, vol. 344, pp. 102–112, 2016.

[15] T. Laursen, Computational Impact and Contact Mechanics, Springer, Berlin, 2002.

[16] P. Le Tallec, C. Rahier, A. Kaiss, Three-dimensional incompressible viscoelasticity in large strains: Formulation and numerical approximation, Computer methods in Applied Mechanics and Engineering, vol. 109, pp. 233–258, 1994.

[17] B.N.J. Persson. Contact mechanics for randomly rough surfaces. Surf Sci Rep, vol. 61(4), pp. 201–27, 2006

[18] S. Reese, S. Govindjee, A theory of finite viscoelasticity and numerical aspects, Int. J. Solids Struct., vol. 9-35, pp. 3455–3482, 1998.

[19] R. A. Schapery, Analytical models for the deformation and adhesion components of rubber friction, Tire Science and Technology (TSTCA), vol. 6, n°1, pp. 3-47, 1978.

[20] H.M. Stanley, T. Kato, An FFT-based method for rough surface contact. J Tribology vol. 119(3), pp. 481, 1997.

[21] A.I. Vakis et al., Modeling and simulation in tribology across scales: An overview, Tribology International, vol. 125, pp. 169–199, 2018.

[22] P. Wagner, Numerical multiscale modelling and experimental validation of low speed rubber friction on rough road surfaces including hysteretic and adhesive effects, Tribology International, vol. 111, pp. 243–253, 2017.

[23] P. Wriggers, P., Computational Contact Mechanics, Springer, Hannover, 2006.

[24] V.A. Yastrebov, G. Anciaux, J.F. Molinari, From infinitesimal to full contact between rough surfaces: Evolution of the contact area, International Journal of Solids and Structures, vol. 52, pp. 83–102, 2015.